QUantitative Imaging of eXtraction of oxygen and TIssue consumption (QUIXOTIC) using venular-targeted velocity-selective spin labeling

Citation: Bolar, D. S., B. R. Rosen, A. G. Sorensen, and E. Adalsteinsson. "QUantitative Imaging of eXtraction of Oxygen and TIssue Consumption (QUIXOTIC) Using Venular-Targeted Velocity-Selective Spin Labeling." Magnetic Resonance in Medicine 66, no. 6 (December 2011): 1550–1562.

As Published: http://dx.doi.org/10.1002/mrm.22946

Publisher: John Wiley & Sons, Inc

Persistent URL: http://hdl.handle.net/1721.1/85922

Version: Author's final manuscript: final author's manuscript post peer review, without publisher's formatting or copy editing

Published in final edited form as:
Magn Reson Med. 2011 December ; 66(6): 1550–1562. doi:10.1002/mrm.22946.

QUantitative Imaging of eXtraction of Oxygen and TIssue Consumption (QUIXOTIC) Using Venular-Targeted Velocity-Selective Spin Labeling

D. S. Bolar[1,2,3,*], **B. R. Rosen**[1,2], **A. G. Sorensen**[1,2], and **E. Adalsteinsson**[1,2,3]

[1]Department of Radiology, Athinoula A. Martinos Center for Biomedical Imaging, Massachusetts General Hospital, Charlestown, Massachusetts, USA

[2]Harvard-MIT Division of Health Sciences and Technology, Harvard Medical School, Massachusetts Institute of Technology, Cambridge, Massachusetts, USA

[3]Department of Electrical Engineering and Computer Science, Massachusetts Institute of Technology, Cambridge, Massachusetts, USA

Abstract

While oxygen extraction fraction (OEF) and cerebral metabolic rate of oxygen ($CMRO_2$) are fundamental parameters of brain health and function, a robust MRI-based mapping of OEF and $CMRO_2$ amenable to functional MRI (fMRI) has not been established. To address this issue, a novel method called QUantitative Imaging of eXtraction of Oxygen and TIssue Consumption, or QUIXOTIC, is introduced. The key innovation in QUIXOTIC is the use of velocity-selective spin labeling to isolate MR signal exclusively from postcapillary venular blood on a voxel-by-voxel basis. Measuring the T_2 of this venular-targeted blood allows calibration to venular oxygen saturation (Y_v) via theoretical and experimental T_2 versus blood oxygen saturation relationships. Y_v is converted to OEF, and baseline $CMRO_2$ is subsequently estimated from OEF and additional cerebral blood flow and hematocrit measurements. Theory behind the QUIXOTIC technique is presented, and implications of cutoff velocity (V_{CUTOFF}) and outflow time parameters are discussed. Cortical gray matter values obtained with QUIXOTIC in 10 healthy volunteers are Y_v = 0.73 ± 0.02, OEF = 0.26 ± 0.02, and $CMRO_2$ = 125 ± 15 μmol/100 g min. Results are compared to global measures obtained with the T_2 relaxation under spin tagging (TRUST) technique. The preliminary data presented suggest that QUIXOTIC will be useful for mapping Y_v, OEF, and $CMRO_2$, in both clinical and functional MRI settings.

Keywords

cerebral metabolic rate of oxygen; arterial spin labeling; velocity selective; oxygen extraction fraction

The rate of oxygen consumption in brain cells is known as the cerebral metabolic rate of oxygen ($CMRO_2$) and is an important indicator of brain health and function (1). As oxygen is not produced endogenously in the brain, it must be continuously supplied to meet metabolic demands. Cerebral blood flow (CBF) fulfills this requirement by delivering oxygen via hemoglobin, the principal oxygen carrier in the body. The ratio of oxygen

*Correspondence to: D. S. Bolar, Ph.D., MIT, Building 36-792, 77 Massachusetts Avenue, Cambridge, Massachusetts 02139. dbolar@nmr.mgh.harvard.edu.

consumption to oxygen delivery is called the oxygen extraction fraction (OEF). OEF can be expressed in terms of $CMRO_2$ and CBF (2,3) in the following manner:

$$OEF = \frac{\text{oxygen consumption}}{\text{oxygen delivery}} = \frac{CMRO_2}{[Hb_{total}] \cdot CBF \cdot Y_a} \quad [1]$$

where $[Hb_{total}]$ is the total concentration of hemoglobin in blood and Y_a is the arterial oxygen saturation.

One of the main difficulties in measuring OEF and $CMRO_2$ with in vivo ^1H MRI is the lack of a direct contrast mechanism. However, as hemoglobin modulates MR signal relaxivity based on degree of oxygen saturation (Y), the possibility to indirectly assess OEF and $CMRO_2$ arises. Venous oxygen saturation (Y_v) is extrapolated from the MRI signal and used first to compute OEF (3):

$$OEF = \frac{Y_a - Y_v}{Y_a} \quad [2]$$

where arteriolar blood is assumed fully saturated ($Y_a = 1$) or measured independently by pulse oximetry. Following Eq. 1, $CMRO_2$ is then calculated from OEF and additional CBF and hematocrit measurements. As oxygen is typically extracted as blood traverses the capillary network, Y_v measurements focused at the distal end of the network (i.e., in postcapillary venules) will yield spatially specific OEF and $CMRO_2$ estimates.

One class of methods to measure Y_v uses phase contrast imaging to examine magnetic susceptibility differences between veins and surrounding tissue (4-7) and uses simple, first-principle models to relate phase changes to Y_v. These methods have the advantage of straightforward acquisitions via standard MRI sequences, but require manually visualizing vessels, limiting use in measuring regional or voxelwise Y_v. A second class of methods (8,9) invokes an MRI signal model that quantifies Y_v based on dHb-induced signal loss in extravascular tissue. One such approach developed by An et al. uses a single compartment tissue model to produce OEF (8) and $CMRO_2$ (10) maps. He and Yablonskiy (9) have introduced “quantitative BOLD” which considers a multiple-compartment model and accounts for tissue, blood, and cerebrospinal fluid (CSF) signal and similarly produces OEF maps. This latter approach is especially promising and has been recently used in assessing change in OEF during functional stimulation (11).

A third class of methods to measure Y_v implements an intravascular T_2-based approach and has shown promise in functional MRI (fMRI) settings. This approach uses a theoretically and empirically derived relationship between blood transverse (T_2) relaxation time and blood oxygen saturation (Y) (2). Specifically measuring Y_v requires selective targeting of blood in the venous circulation, without partial voluming with tissue, CSF, or other brain constituents. Isolating this pure venous blood signal, however, has been a major challenge for existing techniques.

As a consequence, intravascular methods require strict selection criteria to identify voxels containing exclusively venous blood. Methods presented by Oja et al. (3) and Golay et al. (12), for example, require functional activation experiments to identify candidate voxels, and of these, only a subset can be used to calculate Y_v. Moreover, because of resolution limitations, usable voxels are typically found only in larger venous vessels. As blood oxygenation in these larger vessels represents oxygen exchange of all supplying capillaries

in a large surrounding region, these techniques have fundamental limitations on spatial specificity. Voxelwise Y_v is unfortunately not feasible.

More recently, Lu and Ge have proposed T_2 relaxation under spin tagging (TRUST) MRI and measure Y_v in the sagittal sinus (13). TRUST-MRI delivers a pure blood signal, free from partial volume effects, by using a spin-labeling approach to eliminate static tissue and CSF via control–tag subtraction. While TRUST is an important advance for T_2-based, Y_v methodology, only global estimates are possible, as blood signal is isolated from the largest cerebral veins (i.e., the sagittal sinus). As such, TRUST Y_v measurements are limited to the terminal draining veins; regional Y_v information is consequently lost.

Our work uses the intravascular T_2-based approach but addresses the largest obstacle for localized measurements: the isolation of postcapillary venular (PCV) blood signal. A novel excitation scheme is proposed that uses velocity-selective spin labeling (VSSL) to isolate PCV blood signal. In principle, the methodology uses velocity-sensitive pulses to exploit heterogeneous blood velocities in the vascular tree and subsequently create a flow-dependent venular blood component that persists after control-tag subtraction. This sequence incorporates T_2 preparation-based technology, acquires PCV blood-weighted images at effective echo times, and exponentially fits these data to estimate PCV blood T_2. $T_{2,blood}$ versus Y curves (with hematocrit as an independent parameter) are then generated from theoretical models and existing 3 T data and are used to calibrate PCV blood T_2 to Y_v. OEF is then estimated from Y_v and combined with CBF (measured with arterial spin labeling MRI) and hematocrit to quantify $CMRO_2$. This new approach is dubbed QUantitative Imaging of eXtraction of Oxygen and TIssue Consumption or “QUIXOTIC.”

In this study, we perform QUIXOTIC and TRUST-MRI on 10 healthy subjects and compare cortical gray matter (GM) values of T_2, Y_v, OEF, and $CMRO_2$ estimated by QUIXOTIC, with global values estimated by TRUST. We further present representative Y_v, OEF, and $CMRO_2$ quantitative maps and proceed to explore the dependence of Y_v measurements on key QUIXOTIC parameters.

THEORY

Venular-Targeted Velocity-Selective Spin Labeling

The key innovation behind the QUIXOTIC approach is venular-targeted VSSL (VT-VSSL). VT-VSSL allows targeting of MR signal exclusively from the PCV blood compartment, from which T_2 and Y_v can be measured. VT-VSSL applies velocity-sensitive MR pulses to exploit differential velocities and accelerations of blood in the vascular tree, and relies on uniformly forward flow from arteries, through capillaries, to veins. The two-step data acquisition paradigm creates control and tag images with and without the desired venular blood component, respectively. Subsequent pairwise control–tag subtraction eliminates signal from static tissue, CSF, and nonvenular blood compartments, leaving an image exclusively containing blood in the postcapillary venules. The following section describes the details and timing behind this approach.

QUIXOTIC is adapted from velocity-selective (VS) arterial spin labeling (14) and uses similar VS modules to dephase blood spins above a given cutoff velocity. The pulse sequence is summarized schematically in Fig. 1 and executed for both tag and control acquisitions.

The principal component of the QUIXOTIC excitation scheme is the VS module. As a time derivative of position, velocity can be phase encoded by applying bipolar gradient pulses, or equivalently, unipolar pulses separated by a 180° refocusing pulse (15). Inserting this phase-

encoding scheme between two excitation pulses with opposite phase ($90° - 90°$) results in the following radiofrequency (RF) pulse train: $90° - G - 180° - G - 90°$. When applied to laminar flow systems found in noncapillary vasculature of the human circulatory system, the result is a filtering of the magnetization from moving blood spins flowing below a certain cutoff velocity (V_{CUTOFF}) and elimination of magnetization from spins flowing above V_{CUTOFF}, according to:

$$M_z = M_0 \cdot sinc(\beta v) \quad [3]$$

where M_0 is the initial magnetization, v is spin velocity. β is related to the separation (Δ), duration (δ), and amplitude (G) of the bipolar gradient pulses in the following manner:

$$\beta = \gamma G \delta \Delta \quad [4]$$

where γ is the gyromagnetic ratio for protons. The first zero-crossing thus defines V_{CUTOFF} (14,16):

$$V_{CUTOFF} = \frac{\pi}{\beta} = \frac{\pi}{\gamma G \delta \Delta} \quad [5]$$

Figure 2 displays the sinc-filter profile and the ideal velocity filter for comparison.

Instead of using a $90° - G - 180° - G - 90°$ pulse train, which can be implemented with simple hard RF pulses, a four RF and four gradient approach was used (as suggested in Ref. 14):

$$90° - G^{+} - 180° - G^{-} - G^{+} - 180° - G^{-} \overline{-90°} \quad [6]$$

which incorporates adiabatic pulses as the refocusing 180°s. This train offers greater resistance to transmitted field (B_1^+) and static field (B_0) inhomogeneity, water diffusion, and eddy current effects (14,17). Prior investigations using this eight-pulse sequence (14) verify its superior performance with reduced artifacts compared to data acquired with the simpler $90° - G - 180° - G - 90°$ train (16). The final VS train is shown in Fig. 3; for perfect spin-echo refocusing, the adiabatic refocusing pulses are symmetrically spaced.

The difference between the QUIXOTIC tag and control acquisitions lies in the second VS module. While the tag acquisition applies a user-defined cutoff velocity (V_{CUTOFF}) for both VS module I (VS1) and VS module II (VS2), the control uses V_{CUTOFF} for VS1, but disables velocity selection for VS2 (i.e., flowing spins are unaffected, V_{CUTOFF} = infinity). Incorporated into VS2 is a T_2-preparation module (18,19), allowing T_2 estimation via data acquisition at multiple echo times. An important feature of the sequence is an inversion pulse at TO_1, which compensates for adverse effects of T_1 relaxation that could potentially introduce unwanted signal from arterial blood.

To introduce properties of this sequence, we first neglect T_1 relaxation and the TO_1 inversion pulse. Figure 4 provides an idealized cartoon depicting blood spins in the circulation for both control and tag acquisitions, their history during the pulse sequence timing, and the final contribution in the subtracted image. At $t = 0$, before VS1, all blood (arterial, venous, capillary) is relaxed (Fig. 4a). Strong velocity weighting (low V_{CUTOFF}) is then applied during VS1 for both tag and control, selecting for slow moving spins in small

arterioles, capillaries, and small venules ($V < V_{CUTOFF}$) but dephasing faster moving spins in larger vessels ($V > V_{CUTOFF}$) (resulting in a loss of signal, Fig. 4b). Notably, this large-vessel signal is eliminated on both sides of the circulation. After VS1, the outflow time (TO) allows the targeted blood to flow out of the small vessel compartments and accelerate into larger venular vasculature (Fig. 4c). VS2 is then applied at TO. This time, however, the tag and control acquisition experience different velocity weighting: the tag sees velocity selection at V_{CUTOFF}, but the control experiences no velocity weighting. Spins that have accelerated above V_{CUTOFF} during TO are dephased by the tag acquisition but left unaltered in the control (Fig. 4d). As imaging starts immediately after VS2, subtraction of tag from control yields an image weighted to blood that has accelerated from below V_{CUTOFF} to above V_{CUTOFF}, during TO (Fig. 4e). Assuming flow always progresses from arteries to capillaries to veins, these spins are venous only. Signal from other sources (static, CSF, nonvenular blood) is eliminated via subtraction. If V_{CUTOFF} and TO are chosen properly, signal from PCV blood is exclusively targeted.

Due to the tortuous nature of human vasculature, the spatial direction of flow naturally varies as blood migrates from arteries to capillaries to veins. This phenomenon, however, is not expected to appreciably affect the venular selectivity of the VT-VSSL experiment for the following reasons: first, as phase encoding does not occur during TO (the longest interval of the experiment), the directional changes during this interval have no impact on velocity selection. Conversely, directional changes during the VS module will affect selectivity. However, because the encoding time is so short (approximately 20 ms), directional changes are both minor and expected to average out given the broad distribution of vessel orientation in a parenchymal voxel. In this way, as long as there exists some flowing blood with a velocity component aligned with the encoding direction greater than V_{CUTOFF}, VT-VSSL can occur. A more detailed discussion of the directional sensitivity of the VS module is discussed by Frank et al. (20).

T_1 relaxation complicates the idealized model depicted in Fig. 4. Spins dephased by VS1 at $t = 0$ experience longitudinal magnetization recovery. Because velocity selection via VS2 occurs only for the tag but not control, spins from unwanted compartments will partially recover in the control, but dephase in the tag at TO+. Without compensation, these unwanted spins will not subtract completely, and QUIXOTIC loses venous selectivity. To address this effect, we place an inversion pulse at time TO_1 to null recovering blood at TO; consequently, signal from spins in this unwanted population is eliminated in both control and tag at TO, leaving only desired PCV blood on subtraction.

To generate the PCV blood-weighted maps at different echo times, T_2 preparation is integrated into the VS2 pulse train. For the shortest effective echo time (TE_{eff}), the VS2 module is exactly as pictured in Fig. 2. For each successive TE_{eff}, an additional pair of adiabatic 180° pulses is added between the flip-up 90° pulse and first VS gradient lobe. In this way, the duration of VS2 will increase by ΔTE_{eff} for each successive TE_{eff}. Importantly, this is done while keeping an identical readout onset time regardless of TE_{eff}. Using T_2 preparation and fixing the readout module timing makes the T_2 encoding flow insensitive; in other words, images at successive TE_{eff} should differ only by T_2 weighting, not by volume of blood delivered during TO (18).

Signal intensity (SI) in the acquired blood-weighted images can be plotted versus TE_{eff} and fit exponentially on a voxel-by-voxel basis to generate T_2 maps of PCV blood. T_2 values are then calibrated to Y_v and Eqs. 1 and 2 can be used compute $CMRO_2$ and OEF. The following sections explain these steps in greater detail.

T_2 Estimate: Determination of Effective Echo Times (TE_{eff})

Proper estimates of T_2 from fitting SI versus TE_{eff} data depend on accurate estimates of TE_{eff} at each successive acquisition. Ideally, TE_{eff} is equal to the duration of the T_2-preparation module, assuming pure T_2 relaxation and very short refocusing pulses. In practice, however, magnetization does not experience pure T_2 decay during the hyperbolic secant refocusing pulses (18), and further, despite a long repetition time (TR; 4 s), a small amount of residual T_1 contamination is present from spins that have not completely relaxed. To reduce the impact of such biases to the T_2 estimate, we derived a small adjustment to the nominal echo spacing and applied the resulting effective echo spacing, ΔTE_{eff}, for T_2 estimation from the measured data. Specifically, we simulated the pulse sequence using the Bloch equation, assumed T_1 and T_2 decay during the hyperbolic secant refocusing pulses, and estimated the ΔTE_{eff} appropriate for our pulse sequence. The T_1 and T_2 used for the simulation were 1660 and 70 ms, respectively, which are approximate T_1 and T_2 values for deoxygenated blood at 3 T (13,21).

$T_{2,blood}$ Versus Y Calibration

The relationship between transverse relaxation time of blood and blood oxygen saturation (Y) was first examined in the early 1980s, by Thulborn et al. (22). In years following, a parametric model based on the Luz–Meiboom model of spin relaxation during two-compartment exchange (in this case, between plasma and the red blood cell) was derived to fit experimental data measuring variations of $T_{2,blood}$ and blood oxygen saturation. Such work enabled MRI-based measurements of oxygen saturation in vivo (23). In 1998, Van Zijl et al. proposed a fundamental theory for T_2-based signal changes in perfused tissue and presented a quantitative model linking T_2 relaxation of blood to physiologic parameters including Y (2,12). This expression can be written in terms of $T_{2,\,blood}$, Y, and hematocrit (Hct) in the following form:

$$\frac{1}{T_{2,blood}} = A + \mathrm{Hct}\left[(B + C(1-Y)) + (1-\mathrm{Hct})(D + E(1-Y))^2\right] \quad (7)$$

where A, B, C, D, and E represent lumped biophysical parameters related to susceptibility differences between the red blood cell and plasma, water relaxation rates in the red blood cell and plasma, and the spacing between 180° RF pulses in a CPMG spin-echo module (τ_{CPMG}).

Fit of available Y versus $T_{2,blood}$ data at 3 T obtained from in vitro bovine blood (3 T, Carr Purcell Meiboom Gill (CPMG) multiecho T_2 sequence, τ_{CPMG} = 10 ms, courtesy of P. van Zijl and C. Clingman, Johns Hopkins University), yielded values for A, B, C, D, E, that we used in our work. Using these values, Y versus T_2 curves (with Hct as an independent parameter) were generated. Bovine blood has the same properties as human blood in terms of hemoglobin content, erythrocyte size, and diffusional permeability and is expected to have similar MR relaxation properties (12). It has been successfully used in the past for similar calibration experiments (12,13,24).

Calculation of $CMRO_2$ From Y_v

Once Y_v is obtained, $CMRO_2$ and OEF can be calculated by using Eqs. 1 and 2, with the final hematocrit measurement used to calculate the total hemoglobin concentration:

$$[\mathrm{Hb_{tot}}] = \frac{\mathrm{Hct}}{3.0(\mathrm{mL/g}) \cdot 0.016125(\mathrm{g}/\mu\mathrm{mol})} \quad [8]$$

MATERIALS AND METHODS

QUIXOTIC was used to evaluate Y_v, OEF, and $CMRO_2$ in healthy volunteers. The protocol was approved by the University's Committee of Using Humans as Experimental Subjects. Ten young (22–32 years) nonsmoking, healthy subjects (six females, four male) were scanned at 3 T (Siemens Tim Trio, Erlangen, Germany) with the following MRI protocol:

1. T_1-weighted magnetization prepared rapid acquisition gradient recalled echo (MP-RAGE) image for anatomical localization: voxel size = 1 mm^3, matrix size = 256 × 256 × 68, acquisition time = 4 min 32 s.
2. VT-VSSL blood-weighted imaging: V_{CUTOFF} = 2.0 cm/s (G = 1.6 G/cm, Δ = 17 ms, δ = 2 ms, duration between 180 pulses (τ_{180}) = 10 ms, x-directed), TO_1 = 400 ms (assuming $T_{1,blood}$ = 1664 ms at 3 T; Ref. 3), TO = 725 ms, τ_{CPMG} of T_2-preparation module = 10 ms. A gradient recalled echo planar imaging (EPI) readout was used for both tag and control image acquisitions: echo time = 12 ms, phase partial Fourier 6/8, bandwidth = 2232 Hz/pixel, matrix size = 64 × 64, single slice, voxel size = 3.9 × 3.9 × 10 mm^3, TR = 4 s. Eighty measurements were acquired (40 control, 40 tag images), for an imaging time of 5 min 30 s per TE_{eff}. Either five or six TE_{eff}s (depending on specific absorption rate constraints) were acquired with a ΔTE_{eff} = 18.4 ms.
3. Pulsed arterial spin label (ASL) CBF imaging: PICORE/Q2tips (25), TI_1 = 700 ms, TI_1 stop time = 1400 ms, TI_2 = 1600 ms, pulsed ASL gap = 10 mm, Tag thickness = 160 mm, TR = 2000 ms, one slice, 60 measurements, acquisition time = 2 min. EPI parameters are as listed for 3). M_0 calibration scan had identical imaging parameters, except ASL-specific pulses were disabled, and only one measurement was acquired.
4. Double inversion recovery (DIR) for GM-only images: TI_1 = 3700 ms, TI_2 = 4280 ms, one slice, one measurement, with EPI parameters as listed in 3.
5. TRUST sagittal sinus blood imaging: tag thickness = 50 mm, gap = 10 mm, TI = 800 ms, TR = 8 s, eight measurements per TE_{eff} were acquired, ΔTE_{eff} = 18.0 ms, one slice. EPI parameters and T_2 preparation are as listed for 2. Hyperbolic secant pulses identical to those in QUIXOTIC were used for TRUST T_2 preparation.

Automatic alignment routines (26) were used to ensure similar slice placement among all subjects. A slightly oblique-axial slice-of-interest was prescribed immediately superior to the corpus callosum for acquisitions two to four and contained a significant fraction of GM. A different oblique-axial slice intersecting the sagittal sinus was positioned for acquisition five (TRUST).

Venular blood-weighted imaging comprised the bulk of the scan session and the imaging time for the full protocol was less than an hour. Data were acquired at six TE_{eff}s if possible, but in four subjects, specific absorption rate constraints imposed a limitation of only five TE_{eff}s. To test the reproducibility, we performed the VT-VSSL experiment twice on two of the volunteers. These volunteers remained in the scanner for an additional 30 min for the second VT-VSSL acquisition. The two VT-VSSL trials were spaced approximately half an hour apart and used identical scan parameters.

After MRI scanning, hematocrit was measured via finger prick blood sample using the Ultracrit device (Separation Technologies, Altamonte Springs, FL). O_2 saturation was measured with a pulse oximeter (8600FO Pulse Oximeter, Magmedix, Fitchburg, MA).

The data from each TE_{eff} acquisition were corrected for bulk motion and then subtracted, control minus tag, in a pairwise fashion. The subtraction series was averaged to produce mean PCV-weighted images. The DIR image was used as a GM mask, within which venular blood SI from cortical GM tissue was measured. PCV blood signal intensities from the entire cortical GM region were plotted versus TE_{eff} to provide whole-slice cortical GM measurements. The plots were then exponentially fit using a Levenberg–Marquardt least squares optimization method to measure the T_2 relaxation parameter for whole-slice cortical GM, and the standard error of the estimated parameter (SEE) assuming a *t*-distribution was computed.

The TRUST acquisitions were similarly subtracted in a pairwise fraction and averaged to produce maps containing sagittal-sinus only blood at the five TE_{eff}s. The mean SI from the six brightest sagittal sinus voxels blood was plotted versus TE_{eff} and fit to estimate sagittal-sinus blood T_2. The SEE assuming a *t*-distribution was computed.

T_2 values from both VT-VSSL and TRUST analyses were then calibrated to Y_v using curves generated with Eq. 7, incorporating the hematocrit measured from the volunteer. As VT-VSSL data derive mostly from blood in small vessels, the T_2 versus Y calibration was calculated using the microvascular hematocrit (i.e., by multiplying the measured hematocrit by 0.85 to correct for hematocrit differences between small and large vessels; Ref. 27). This correction was not needed for the TRUST calibration curves, as the source of venous blood was exclusively from the large sagittal sinus. Y_a was taken as the oxygen saturation measured with the pulse oximeter; Eq. 2 was then used to calculate OEF.

To obtain $CMRO_2$ from Eq. 1, CBF was estimated by ASL MRI, with a VT-VSSL matching slice prescription. The ASL data were similarly analyzed to generate blood flow-weighted images, via subtraction, motion correction, and signal averaging. These images were calibrated to absolute CBF maps by using the local tissue proton density provided by the M_0 scan (28). GM CBF was estimated from the region segmented by the DIR GM mask. White matter (WM) CBF was estimated from the remaining, nonsegmented brain region. The WM and GM CBF values were used to calculate whole brain CBF, by assuming a whole-brain WM:GM ratio of 0.675:1 (29). With these additional CBF measurements, and by using hematocrit to estimate $[Hb_{total}]$, both QUIXOTIC (GM) and TRUST (whole brain) $CMRO_2$ were, respectively, calculated.

To demonstrate feasibility of using QUIXOTIC to create quantitative Y_v, OEF, and $CMRO_2$ maps, raw data from a representative subject were smoothed with a 10 mm full width at half maximum (FWHM) Gaussian kernel and fit for T_2, but this time on a voxel-by-voxel basis (as opposed to using a GM mask). The resultant T_2 map was subsequently calibrated to generate quantitative Y_v and OEF maps, using aforementioned calibration curves. Finally a $CMRO_2$ map was generated by multiplying the OEF map with the absolute ASL-CBF map on a voxel-by-voxel basis and incorporating $[Hb_{total}]$ and Y_a (as described in Eq. 1).

Finally, to briefly investigate effects of the two key QUIXOTIC parameters, TO and V_{CUTOFF}, on the measured Y_v, three of the original 10 subjects returned for a separate, additional imaging session and were scanned at five different TOs (525, 625, 725, 825, and 925 ms) with a fixed V_{CUTOFF} of 2.0 cm/s, and four different V_{CUTOFF}s (1.5, 2.0, 3.0, and 4.0 cm/s) with a fixed TO of 725 ms. As using the standard QUIXOTIC approach to explore this parameter space would have resulted in impractical scan times (approximately 5 h), a faster variant (a so-called “turbo QUIXOTIC” approach) was developed and incorporated. Turbo QUIXOTIC uses a turbo spin echo EPI readout to generate images at multiple echo times per TR; this contrasts the standard T_2 preparation approach, which acquires a single TE_{eff} image per TR. Turbo QUIXOTIC thus obtains the full set of images for a particular

TO-V_{CUTOFF} combination in a single scan, allowing data for the above parameter exploration to be acquired in less than an hour. Specific imaging parameters were: TE_{eff} = 22.6 ms, bandwidth = 3256 Hz/pixel, matrix size = 32 × 32, single slice, voxel size = 7.8 × 7.8 × 10 mm^3, TR = 4 s, generalized autocalibrating partially parallel acquisition with 3× acceleration. Eighty measurements were acquired at four TE_{eff}s, resulting in 40 control/40 tag per TE_{eff}, and an imaging time of 5 min 30 s per TO/V_{CUTOFF} combination. A resolution-matched double IR image was acquired for GM segmentation; subsequent data processing to calculate Y_v was performed as described for the standard approach.

Data processing was done in Neurolens (www.neurolens.org) software and with custom Matlab (MathWorks, Natick, MA) routines.

RESULTS

Figure 5 shows the mean difference images for the VT-VSSL and TRUST acquisitions at five effective TEs for a representative subject. The signal in the VT-VSSL images is our estimate of the PCV blood, which decays with a T_2 time constant that depends on the blood oxygenation level.

Figure 6a and b show the ASL-CBF map and the GM mask, respectively. Figure 6c displays the slice orientation of the preceding acquisitions, overlaid on a high resolution midsagittal section from the MP-RAGE scan.

Figure 7 shows the whole-slice cortical-GM SI versus TE_{eff} (QUIXOTIC) and sagittal sinus SI versus TE_{eff} (TRUST) on a semilog scale for all subjects, including the fitted lines for T_2 estimates. All line fits had high R^2 values: ≥0.95 for QUIXOTIC and ≥0.99 for TRUST. To improve the figure readability and highlight the relevant parameter (slope of line fits), the vertical offset of each line in each technique has been normalized. The *y*-intercept estimates the volume of tagged blood that remains after subtraction within the sagittal sinus and GM voxels for TRUST and QUIXOTIC, respectively, but does not enter the OEF or $CMRO_2$ estimates.

Figure 8 shows calibration curves generated with Eq. 7 for the same subject. Values of *A*, *B*, *C*, *D*, and *E* for Eq. 7 were found as 1.09 s^{-1}, 11.26 s^{-1}, −7.96 s^{-1}, 1.08 $s^{-1/2}$, and 16.54 $s^{-1/2}$, respectively. Two curves are depicted for both microvascular and macrovascular hematocrit, to be used for QUIXOTIC and TRUST analyses, respectively. Lower hematocrit shifts the $T_{2,blood}$ versus *Y* curve to the left, resulting in lower estimated oxygen saturations (*Y*) for a fixed measured $T_{2,blood}$ value.

Figure 9 shows the Y_v, OEF, and $CMRO_2$ maps for the same representative subject, created by applying QUIXOTIC theory on a voxel-by-voxel basis. Y_v and OEF is seen to be relatively uniform across the entire brain, while the $CMRO_2$ map shows substantially higher values in the GM cortex, compared to the interior WM.

Figure 10a and b show Y_v versus TO and Y_v versus V_{CUTOFF}, respectively, for the parameter exploration data acquired with turbo QUIXOTIC in the three reimaged subjects. These data show the dependence of Y_v on these parameters; error bars on the individual data points represent the SEE (roughly ± 1% for all data points). According to Fig. 9a, Y_v is relatively stable across the chosen range of TO values (mean coefficient of variation across TO trials = 1.8 ± 0.4%), with a very slight decreasing trend (mean slope of linear fits, ΔYv/ΔTO = −0.007/100 ms). Fig. 9b, however, suggests substantially more variation in Y_v across the V_{CUTOFF} range (mean coefficient of variation across TO trials = 4.2 ± 2.4%); more importantly, there seems a more pronounced downward trend in Y_v as V_{CUTOFF} increases

(mean slope of linear fits, $\Delta Yv/\Delta V_{CUTOFF} = -0.03$ s/cm), suggesting dependence of estimated Y_v on the choice of V_{CUTOFF}.

Table 1 summarizes the measured blood relaxation times and the estimated quantitative physiological parameters for the 10 subjects, i.e., T_2, Y_v, OEF, CBF, and $CMRO_2$. These values are shown for QUIXOTIC (regional cortical GM and whole-slice cortical GM) and TRUST (whole brain). The QUIXOTIC estimates were $Y_v = 0.73 \pm 0.02$, OEF = 0.26 ± 0.02 and $CMRO_2 = 125 \pm 15$ μmol of O_2/(100 g min), while TRUST yielded $Y_v = 0.63 \pm 0.02$, OEF = 0.36 ± 0.02, and $CMRO_2 = 125 \pm 18$ μmol of O_2/(100 g min).

Table 2 shows the intrascan test–retest data for subjects 1 and 2, including the percent difference in the quantified parameters. The differences were low in both cases, less than 1% and 5% for subjects 1 and 2, respectively.

DISCUSSION

We have introduced a novel MR technique, QUIXOTIC, to quantify regional OEF and regional $CMRO_2$ and have demonstrated its use in normal volunteers. Our estimates of cortical GM OEF and $CMRO_2$ fall within the expected physiological range and are comparable with those reported by other MRI and positron emission tomography methods (10,30-33). Some studies that measure OEF specifically report values of 35%, 42.6%, 41%, and 40% (34-37), which are slightly higher than the 26% reported here. WM values were not calculated in this investigation, due to low WM SNR in VT-VSSL maps for several subjects.

QUIXOTIC produces venular blood maps by creating flow-derived signal from within the imaging voxel. In principle, this property allows generation of venular blood maps on a voxel-by-voxel basis. By obtaining maps at several effective echo times (T_{eff}), it is possible to fit for T_2 and subsequently obtain voxelwise measures of Y_v, OEF, and $CMRO_2$ (as shown in Fig. 9). Of note, we assumed T_1 and T_2 values of 1660 and 70 ms, respectively, to estimate ΔTE_{eff} via Bloch simulation. Deviations in these assumed values will result in a small bias in the QUIXOTIC measured T_2s of venular blood. To examine this effect more closely, we tested: (a) the range of T_1s from 1560 and 1760 and found a resulting effect of approximately 0.5 ms on estimated T_2, and (b) the range of T_2s between 50 and 90 ms, resulting in an effect of approximately 2.5 ms on measured T_2. Even at the extremes, these small deviations in measured T_2 will result in even smaller deviations on measured Y_v, OEF, and $CMRO_2$ (between 1 and 2%); well within the noise of our measurement.

Outflow Time and Cutoff Velocity (V_{CUTOFF})

Two key parameters define the nature of the QUIXOTIC signal and directly control its spatial specificity, signal-to-noise ratio (SNR), and maximum SNR: cutoff velocity (V_{CUTOFF}) and TO. When taken together, V_{CUTOFF} and TO determine the extent of the velocity-selected bolus at imaging time by defining its trailing and leading edge, respectively, and subsequently the venular blood component remaining in the subtracted image.

The TO of the QUIXOTIC experiment determines the SNR and spatial specificity of the subtracted venular blood component. During TO, blood spins accelerate above the V_{CUTOFF} threshold and into receiving venular vasculature within the imaging voxel. Imaging signal is created, and intensity increases as these spins begin to fill the imaging voxel. Neglecting T_1 decay, the final SI is directly proportional to the volume of blood that has accelerated above V_{CUTOFF} during TO, while still remaining within the voxel (hereafter termed as “imaging blood volume”). Realistically, however, T_1 decay will have a competing effect on overall SI;

thus in practice, an SNR-optimized TO will consider both imaging blood volume and T_1 decay.

As flowing spins in the velocity-selected bolus disseminate through the tortuous venular microvasculature during TO, they flow deeper into the venous circulation, and the leading edge of the bolus travels further away from capillary sites of gas exchange. As long as these tagged spins do not leave the voxel, oxygen saturation within these pools properly represents oxygen exchange of their capillary sources. Spatial specificity is preserved, and imaging blood volume is exactly the product of venular outflow and TO.

V_{CUTOFF} determines the maximum possible SNR of the venular blood component in the final image, by defining the maximum available vascular volume that can be occupied by the venular bolus. As blood velocity is closely related to vessel caliber, V_{CUTOFF} not only defines the cutoff blood velocity, but also determines how far into the venous vascular tree the trailing edge of imaged bolus is located. A low V_{CUTOFF} means that trailing edge originates closer to the distal end of the capillary bed, while a high V_{CUTOFF} means that the trailing edge originates closer to terminal draining veins. As V_{CUTOFF} increases, the trailing edge moves farther along the venous vascular tree, effectively reducing the remaining vascular voxel volume that can be filled by tagged blood. In this way, V_{CUTOFF} sets a hard limit to the maximum imaging blood volume that can occupy a voxel, with lower V_{CUTOFF}s offering higher SI at the optimal TO. A V_{CUTOFF} just above capillary blood velocities is the ideal choice. A V_{CUTOFF} lower than capillary velocities is undesirable for three reasons: (1) VS theory assumes laminar flow, not capillary plug flow (14), for proper velocity filtering, (2) as V_{CUTOFF} decreases, the relaxed blood pool available to flow above V_{CUTOFF} will at some point become small, also resulting in SNR reduction, and (3) when large velocity weighting is applied, tissue and CSF water diffusion becomes a contaminating source of signal (14). Notably, prior VS-ASL studies have indicated that a $V_{CUTOFF} \geq 2$ cm/s will result in subtractions free from diffusion contamination (14,38).

Based on the above considerations and pilot data (39), we chose $V_{CUTOFF} = 2$ cm/s and TO = 725 ms. These choices yield sufficient SNR in the final venular blood images for cortical analysis at 3 T and maintain high spatial specificity. As seen in Fig. 5, venular blood signal appears well-matched to cortical gyri, with minimal blurring, which can be appreciated by comparing the venular blood-weighted images to the CBF and DIR images in Fig. 6.

In this initial demonstration of QUIXOTIC, we performed limited exploration of the dependence of Y_v on TO and V_{CUTOFF} parameters. This required development of the turbo QUIXOTIC variant, which allowed the considerably shorter scan times needed to accommodate a multiparameter exploration. Turbo QUIXOTIC differs from the standard approach by using a turbo spin echo readout to acquire data at multiple effective TEs per scan, instead of only at a single TE_{eff}. Consequently, turbo QUIXOTIC generates all necessary images for T_2 fitting and subsequent analysis in a single scan, thereby reducing the required imaging time by several fold. In this specific implementation, the total acquisition time for a fixed TO and V_{CUTOFF} combination decreased from 25–30 min to 5.5 min. This dramatic reduction in imaging time enabled us to explore several TO and V_{CUTOFF} combinations in a single scan session. We used this approach in three subjects to see how calculated Y_v varied across (1) a range of TOs at a fixed $V_{CUTOFF} = 2$ cm/s, and (2) a range of V_{CUTOFF}s at a fixed TO = 725 ms. Figure 10 shows the calculated Y_v across these parameter ranges. The average slope of −0.007 per 100 ms for the Y_v versus TO data (Fig. 10a) suggests that the measured Y_v is robust to variations in TO; across a range of 400 ms, this translates to a less than 3% variation in Y_v. On the other hand, Fig. 10b indicates a more significant dependence of Y_v on the V_{CUTOFF} parameter; an average slope of −0.03 per cm/s suggests that as V_{CUTOFF} increases over a range of 4 cm/s, the measured Y_v will decrease by

12%. Whether this effect is an artifact of increased diffusion weighting at lower V_{CUTOFF}s, or a consequence of the physiologic properties of the isolated venular pool that survives after velocity encoding, is the topic of detailed future QUIXOTIC studies.

An additional positive consequence of using turbo QUIXOTIC is that R^2 for all T_2 fits was >0.99, with an SEE of roughly 3 ms; this marks a substantial improvement over the standard QUIXOTIC variant. We postulate that this improvement is due the fact that turbo QUIXOTIC is considerably more resistant to both bulk and physiological motion for the following reasons: (1) motion affects all TE_{eff} points equally in turbo QUIXOTIC due to parallel TE_{eff} acquisition, whereas it will affect each TE_{eff} point differently in standard QUIXOTIC (due to serial TE_{eff} acquisition) leading to noiser SI versus TE_{eff} data and (2) total scan time is significantly shorter in turbo QUIXOTIC, resulting in less motion artifact across the experiment. Due to higher quality data and reduced scan time, we expect turbo QUIXOTIC to eventually be the variant of choice for Y_v, OEF, and $CMRO_2$ voxel-by-voxel mapping.

Comparison of QUIXOTIC and TRUST Measurements

Values of OEF and $CMRO_2$ estimated with QUIXOTIC fall within the physiologic range and are in good agreement with other PET and MR measures in the literature. The key physiologic parameter measured by QUIXOTIC is local venular oxygen saturation Y_v, which shows low measurement variability across 10 subjects (coefficient of variation = 0.03). Of note, however, is that the whole-slice cortical GM Y_v measurements by QUIXOTIC were significantly higher than sagittal sinus Y_v measured with TRUST (0.73 vs. 0.63 for QUIXOTIC and TRUST, statistically different at $P < 0.00001$, paired *t*-test). Moreover, the 95% CI for the true difference in Y_v between the techniques lies between 0.08 and 0.11, suggesting a systematic bias between the two techniques. This Y_v discrepancy translates into a lower OEF for QUIXOTIC, compared to TRUST (0.26 vs. 0.36). Table 1 highlights these differences, where whole-brain Y_v measured with TRUST is on average 14% less than the single-slice cortical GM Y_v measured with QUIXOTIC.

Sources of bias may originate from the QUIXOTIC technique itself. Among these is contamination of the venular-derived VS bolus by arterial blood, which could manifest in at least two different ways. As mentioned in Theory section, initially dephased arterial blood will experience T_1 recovery after VS1. In an effort to prevent this blood from giving rise to signal in the final subtraction, we inserted a single inversion pulse at a time TO_1, which in theory should null this arterial component. TO_1 is based on an assumed $T_{1,blood}$ (21); if the true $T_{1,blood}$ differs significantly from this assumed value, the inversion null may not be effective, leading to an arterial contribution in the final subtracted signal. As the T_2 of fully oxygenated arterial blood is greater than 150 ms (as empirically determined by ASL-based experiments using an identical T_2-preparation module), a small fractional contribution of arterial signal could bias the measured T_2, and subsequently Y_v. To explore this potential contamination source, we implemented and tested a double-inversion approach in QUIXOTIC (data not shown), which dramatically improves nulling robustness and reduces signal across a much wider T_1 range (but imposes an additional specific absorption rate penalty). Comparing the single- and double-inversion variants of QUIXOTIC did not yield a substantial change in measured T_2, leading us to conclude that arterial contamination by incomplete T_1 nulling is not a dominant source of error.

Another possibility for arterial contamination could be attributed to the nonideal velocity selection profile. While the ideal velocity-selective profile perfectly preserves signal from all spins below V_{CUTOFF} and dephases all spins above V_{CUTOFF}, the actual VS profile follows a sinc envelope as a function of spin velocity (Fig. 2). Consequently, the final VS bolus will also have a sinc-like shape, including side lobes that extend into the arterial side

of the circulation. As TO increases, the VS bolus will move further into the venous circulation, and the side lobes on the arterial side become smaller, resulting in less contamination. This potential contamination source was explored with turbo QUIXOTIC in three subjects, and as previously mentioned, there was little variation in measured Y_v across a TO range of 400 ms. These turbo QUIXOTIC data suggest that this source of arterial contamination is not a large source of bias in QUIXOTIC.

A second potential source of bias in measuring Y_v with QUIXOTIC is the inevitable diffusion weighting in the experiment. The combination of gradient and RF pulses that allow velocity selection will at the same time lead to (mild) diffusion weighting. As the control image acquisition involves turning off the gradients during VS2, the control image will not be diffusion weighted, while the tag image will be slightly diffusion weighted. The subsequent subtraction map will have some degree of diffusion weighting, thus introducing both tissue and CSF components into the otherwise pure venular blood-weighted images. This problem was explored by Wong and colleagues for VS-ASL (14,40). Both studies concluded that diffusion effects were minimal, due to the weak gradients (G), short gradient durations (δ), and large gradient separation (Δ) used in the VS module. In our specific experiments, b value was calculated to be approximately 1 s/mm^2, leading to less than 0.07% attenuation in tissue (D_{tissue} = 0.0008 mm^2/s) and less than 0.020% attenuation in CSF (D_{CSF} = 0.0024 mm^2/s), given CSF and tissue fractions of up to 95% (41) and up to 10% (42), respectively. Given that the subtracted blood-weighted signal is roughly 2% of the original signal, we expect less than 4% error from diffusion effects at TE_{eff} = 0. However, because the T_2s of CSF and tissue are longer than the T_2 of deoxygenated blood, diffusion-based effects could become more prominent at longer effective echo times. Results from the turbo QUIXOTIC parameter exploration are consistent with this idea. As seen in (Fig. 10b). Y_v (and thus T_2) increases with decreasing V_{CUTOFF}. One explanation for this phenomenon is that lower V_{CUTOFF}s result in images containing non-negligible signal from diffusing tissue/CSF water. As water from these sources has a larger T_2 than venular blood water, the measured T_2 (and subsequent Y_v) could be biased upward. In this limited turbo QUIXOTIC dataset, it is also interesting to note that as V_{CUTOFF} increases (and diffusion effects abate), parenchymal Y_v values trend towards global Y_v values measured by TRUST. Further studies are needed to investigate these effects in greater detail.

Finally, a physiological source to the TRUST-QUIXOTIC Y_v discrepancy cannot be ruled out, especially based on the dramatic difference in the location and size of the targeted vessels in each technique. TRUST measures Y_v from the final draining vein of the cerebral circulation, the sagittal sinus. At this stage of the circulation, oxygen exchange is complete, and blood is expected to be at its lowest level of oxygenation. In contrast, QUIXOTIC by design measures oxygenation of blood in venules just distal to draining capillary beds. If extraction is not complete by the time blood reaches the distal end of the capillaries, exchange will continue to occur until equilibrium is reached. Such a phenomenon would result in early venular blood to remain more oxygenated than blood in terminal draining veins, resulting in QUIXOTIC Y_v values greater than TRUST sagittal sinus Y_v values. A more detailed investigation is required to properly determine if such a phenomenon could exist and play role in the TRUST-QUIXOTIC Y_v discrepancy.

An important practical difference between TRUST and QUIXOTIC is SNR. SNR is directly related to the imaging blood volume, which is represented by the vertical intercepts in Fig. 7a. Because of the high fractional blood volume in the sagittal sinus (approximately 1), the imaging blood volume is between one and two orders of magnitude greater in TRUST, compared to QUIXOTIC. In this way, TRUST has a major SNR advantage, affording shorter imaging times and higher precision fits.

While beyond the scope of this article, a brief comment can be made on the feasibility of using QUIXOTIC (and more specifically the turbo QUIXOTIC variant) in functional MRI. The primary advantage offered by QUIXOTIC is the ability to generate a OEF and $CMRO_2$ map every two TR (analogous to how CBF maps are generated in ASL-fMRI). While the TR used in these studies was 4 s, shorter TRs (on the order of 2 ms) are possible, with similar temporal SNR. In this way, similar to functional ASL-MRI, we anticipate useful application of QUIXOTIC in block design and event-related fMRI experiments. One potential confounder is the increase of local CBF during activation; however, we do not anticipate this to cause a large error. While the trailing edge of the VT-VSSL bolus will be closer to the capillary bed during activation, venular blood will still be considered and oxygenation properly represented (substantial venular oxygenation heterogeneity, however, could complicate this picture).

CONCLUSIONS

QUIXOTIC MRI introduces a novel approach to isolate PCV blood signal and subsequently measure cerebral Y_v, OEF, and $CMRO_2$. Values reported for Y_v, OEF, and $CMRO_2$ are comparable with those acquired by other PET and MR studies, and fall within a normal physiological range. Advantages of QUIXOTIC include: (1) QUIXOTIC maps blood in the venous circulation only, with CSF, static tissue, and capillary/arterial blood eliminated; (2) subject to SNR constraints, QUIXOTIC analysis can be performed on a voxel-by-voxel basis, allowing creation of Y_v, OEF, and $CMRO_2$ maps; and (3) QUIXOTIC generates images every two TR, making the technique amenable to functional imaging of Y_v and OEF during block-design and event-related fMRI. To our knowledge, no currently available technique offers all three features. Future studies will explore optimal parameter settings, employ turbo QUIXOTIC for rapid data acquisition, and deploy QUIXOTIC at higher fields for increased SNR.

Acknowledgments

The authors would like to thank Tim Reese and Thomas Benner for their useful discussion about the velocity selective pulse train.

Grant sponsor: Siemens Medical Solutions; Grant sponsor: Division of Health Sciences and Technology Martinos Catalyst Fund; Grant sponsor: Advanced Multimodal Neuroimaging Training Program Grant; Grant sponsor: NIH; Grant number: RO1 EB007942; Grant sponsor: NIH Medical Scientist Training Program Fellowship; Grant number: T32-GM07753; Grant sponsor: NIH Neuroimaging Training Program Grant; Grant numbers: 5-T32-EB001680, 5-R01-EB002066-20; Grant sponsor: Center for Functional Neuroimaging Technologies; Grant number: P41RR14075S10RR023401.

References

1. Berne, RM.; Levy, MN. Physiology. Baltimore, MD: Mosby Year Book; 1993.
2. van Zijl PC, Eleff SM, Ulatowski JA, Oja JM, Ulug AM, Traystman RJ, Kauppinen RA. Quantitative assessment of blood flow, blood volume and blood oxygenation effects in functional magnetic resonance imaging. Nat Med. 1998; 4:159–167. [PubMed: 9461188]
3. Oja JM, Gillen JS, Kauppinen RA, Kraut M, van Zijl PC. Determination of oxygen extraction ratios by magnetic resonance imaging. J Cereb Blood Flow Metab. 1999; 19:1289–1295. [PubMed: 10598932]
4. Haacke E, Lai S, Reichenbach J, Kuppusamy K, Hoogenraad FG, Tackeichi H, Lin W. In vivo measurement of blood oxygen saturation using magnetic resonance imaging: a direct validation of the blood oxygen level-dependent concept in functional brain imaging. Hum Brain Mapp. 1997; 5:341–346. [PubMed: 20408238]
5. Hoogenraad FG, Reichenbach JR, Haacke EM, Lai S, Kuppusamy K, Sprenger M. In vivo measurement of changes in venous blood-oxygenation with high resolution functional MRI at 0.95

tesla by measuring changes in susceptibility and velocity. Magn Reson Med. 1998; 39:97–107. [PubMed: 9438443]

6. Liu Y, Pu Y, Fox PT, Gao JH. Quantification of dynamic changes in cerebral venous oxygenation with MR phase imaging at 1.9 T. Magn Reson Med. 1999; 41:407–411. [PubMed: 10080291]
7. Fernández-Seara MA, Techawiboonwong A, Detre JA, Wehrli FW. MR susceptometry for measuring global brain oxygen extraction. Magn Reson Med. 2006; 55:967–973. [PubMed: 16598726]
8. An H, Lin W. Quantitative measurements of cerebral blood oxygen saturation using magnetic resonance imaging. J Cereb Blood Flow Metab. 2000; 20:1225–1236. [PubMed: 10950383]
9. He X, Yablonskiy DA. Quantitative BOLD: mapping of human cerebral deoxygenated blood volume and oxygen extraction fraction: default state. Magn Reson Med. 2007; 57:115–126. [PubMed: 17191227]
10. An H, Lin W, Celik A, Lee YZ. Quantitative measurements of cerebral metabolic rate of oxygen utilization using MRI: a volunteer study. NMR Biomed. 2001; 14:441–447. [PubMed: 11746936]
11. He, X.; Yablonskiy, DA. Decrease of deoxy-hemoglobin containing blood volume in activated human visual cortex. Proceedings of the 18th Annual Meeting of ISMRM; Stockholm, Sweden. 2010.
12. Golay X, Silvennoinen MJ, Zhou J, Clingman CS, Kauppinen RA, Pekar JJ, van Zij PC. Measurement of tissue oxygen extraction ratios from venous blood T(2): increased precision and validation of principle. Magn Reson Med. 2001; 46:282–291. [PubMed: 11477631]
13. Lu H, Ge Y. Quantitative evaluation of oxygenation in venous vessels using T2-relaxation-under-spin-tagging MRI. Magn Reson Med. 2008; 60:357–363. [PubMed: 18666116]
14. Wong EC, Cronin M, Wu W-C, Inglis B, Frank LR, Liu TT. Velocity-selective arterial spin labeling. Magn Reson Med. 2006; 55:1334–1341. [PubMed: 16700025]
15. Norris DG, Schwarzbauer C. Velocity selective radiofrequency pulse trains. J Magn Reson. 1999; 137:231–236. [PubMed: 10053152]
16. Duhamel G, de Bazelaire C, Alsop DC. Evaluation of systematic quantification errors in velocity-selective arterial spin labeling of the brain. Magn Reson Med. 2003; 50:145–153. [PubMed: 12815689]
17. Reese TG, Heid O, Weisskoff RM, Wedeen VJ. Reduction of eddy-current-induced distortion in diffusion MRI using a twice-refocused spin echo. Magn Reson Med. 2003; 49:177–182. [PubMed: 12509835]
18. Conolly S, Glover G, Nishimura D, Macovski A. A reduced power selective adiabatic spin-echo pulse sequence. Magn Reson Med. 1991; 18:28–38. [PubMed: 2062239]
19. Brittain JH, Hu BS, Wright GA, Meyer CH, Macovski A, Nishimura DG. Coronary angiography with magnetization-prepared T2 contrast. Magn Reson Med. 1995; 33:689–696. [PubMed: 7596274]
20. Frank LR, Lu K, Wong EC. Perfusion tensor imaging. Magn Reson Med. 2008; 60:1284–1291. [PubMed: 19030161]
21. Lu H, Clingman C, Golay X, van Zijl PCM. Determining the longitudinal relaxation time (T1) of blood at 3.0 Tesla. Magn Reson Med. 2004; 52:679–682. [PubMed: 15334591]
22. Thulborn KR, Waterton JC, Matthews PM, Radda GK. Oxygenation dependence of the transverse relaxation time of water protons in whole blood at high field. Biochim Biophys Acta. 1982; 714:265–270. [PubMed: 6275909]
23. Wright GA, Hu BS, Macovski A. 1991 I.I. Rabi Award. Estimating oxygen saturation of blood in vivo with MR imaging at 1.5 T. J Magn Reson Imaging. 1991; 1:275–283. [PubMed: 1802140]
24. Xu F, Ge Y, Lu H. Noninvasive quantification of whole-brain cerebral metabolic rate of oxygen (CMRO2) by MRI. Magn Reson Med. 2009; 62:141–148. [PubMed: 19353674]
25. Luh WM, Wong EC, Bandettini PA, Ward BD, Hyde JS. Comparison of simultaneously measured perfusion and BOLD signal increases during brain activation with T(1)-based tissue identification. Magn Reson Med. 2000; 44:137–143. [PubMed: 10893532]
26. van der Kouwe AJW, Benner T, Fischl B, Schmitt F, Salat DH, Harder M, Sorensen AG, Dale AM. On-line automatic slice positioning for brain MR imaging. Neuroimage. 2005; 27:222–230. [PubMed: 15886023]

27. Eichling JO, Raichle ME, Grubb RL Jr, Larson KB, Ter-Pogossian MM. In vivo determination of cerebral blood volume with radioactive oxygen-15 in the monkey. Circ Res. 1975; 37:707–714. [PubMed: 811413]
28. Cavuşoğlu M, Pfeuffer J, Ugurbil K, Uludag K. Comparison of pulsed arterial spin labeling encoding schemes and absolute perfusion quantification. Magn Reson Imaging. 2009; 27:1039–1045. [PubMed: 19540694]
29. Schnack HG, HE HP, Baaré WF, Staal WG, Viergever MA, Kahn RS. Automated separation of gray and white matter from MR images of the human brain. Neuroimage. 2001; 13:230–237. [PubMed: 11133325]
30. Ishii K, Sasaki M, Kitagaki H, Sakamoto S, Yamaji S, Maeda K. Regional difference in cerebral blood flow and oxidative metabolism in human cortex. J Nucl Med. 1996; 37:1086–1088. [PubMed: 8965174]
31. Ibaraki M, Miura S, Shimosegawa E, Sugawara S, Mizuta T, Ishikawa A, Amano M. Quantification of cerebral blood flow and oxygen metabolism with 3-dimensional PET and 15O: validation by comparison with 2-dimensional PET. J Nucl Med. 2008; 49:50–59. [PubMed: 18077532]
32. Ibaraki M, Sato K, Mizuta T, Kitamura K, Miura S, Sugawara S, Shinohara Y, Kinoshita T. Evaluation of dynamic row-action maximum likelihood algorithm reconstruction for quantitative 15O brain PET. Ann Nucl Med. 2009; 23:627–638. [PubMed: 19562437]
33. Fukuyama H, Ogawa M, Yamauchi H, Yamaguchi S, Kimura J, Yonekura Y, Konishi J. Altered cerebral energy metabolism in Alzheimer's disease: a PET study. J Nucl Med. 1994; 35:1–6. [PubMed: 8271029]
34. Carpenter DA, Grubb RL Jr, Tempel LW, Powers WJ. Cerebral oxygen metabolism after aneurysmal subarachnoid hemorrhage. J Cereb Blood Flow Metab. 1991; 11:837–844. [PubMed: 1874816]
35. Yamauchi H, Fukuyama H, Nagahama Y, Nabatame H, Nakamura K, Yamamoto Y, Yonekura Y, Konishi J, Kimura J. Evidence of misery perfusion and risk for recurrent stroke in major cerebral arterial occlusive diseases from PET. J Neurol Neurosurg Psychiatry. 1996; 61:18–25. [PubMed: 8676151]
36. Zazulia AR, Diringer MN, Videen TO, Adams RE, Yundt K, Aiyagari V, Grubb RL Jr, Powers WJ. Hypoperfusion without ischemia surrounding acute intracerebral hemorrhage. J Cereb Blood Flow Metab. 2001; 21:804–810. [PubMed: 11435792]
37. Diringer MN, Yundt K, Videen TO, Adams RE, Zazulia AR, Deibert E, Aiyagari V, Dacey RG Jr, Grubb RL Jr, Powers WJ. No reduction in cerebral metabolism as a result of early moderate hyperventilation following severe traumatic brain injury. J Neurosurg. 2000; 92:7–13. [PubMed: 10616076]
38. Wu W-C, Wong EC. Intravascular effect in velocity-selective arterial spin labeling: the choice of inflow time and cutoff velocity. Neuroimage. 2006; 32:122–128. [PubMed: 16713716]
39. Bolar, DS.; Rosen, BR.; Sorensen, AG.; Adalsteinsson, E. Quantitative imaging of extraction of oxygen and tissue consumption (QUIXOTIC) using velocity selective spin labeling. Proceedings of the 17th Annual Meeting of the ISMRM; Honolulu, HI. 2009.
40. Wu, W.; Wong, E. The effects of water diffusion and laminar flow on velocity-selective arterial spin labeling. Proceedings of the 26th Annual International Conference of the IEEE Engineering in Medicine and Biology Society; San Francisco, CA, USA. 2004. p. 1884-1887.
41. Buxton, RB. Introduction to functional magnetic resonance imaging. New York: Cambridge University Press; 2002.
42. Donahue MJ, Lu H, Jones CK, Edden RAE, Pekar JJ, van Zijl PCM. Theoretical and experimental investigation of the VASO contrast mechanism. Magn Reson Med. 2006; 56:1261–1273. [PubMed: 17075857]

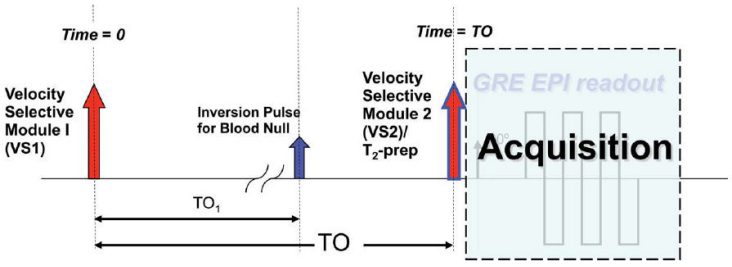

FIG. 1.

QUIXOTIC pulse sequence timing diagram. Sequence is played once for control image generation and repeated for tag image generation. What differs between control and tag acquisition is velocity weighting in the VS2/T_2-preparation module.

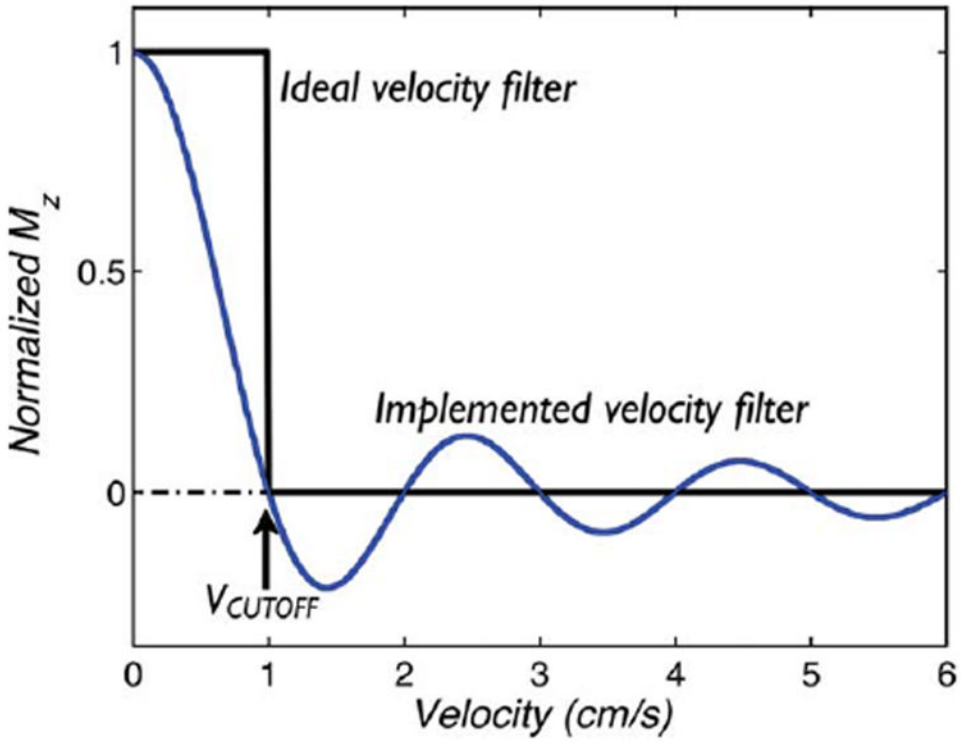

FIG. 2.

M_z modulation produced by velocity selective pulse; ideal filter (black rect function) and implemented filter (blue sinc function), given example V_{CUTOFF} of 1 cm/s. [Color figure can be viewed in the online issue, which is available at wileyonlinelibrary.com.]

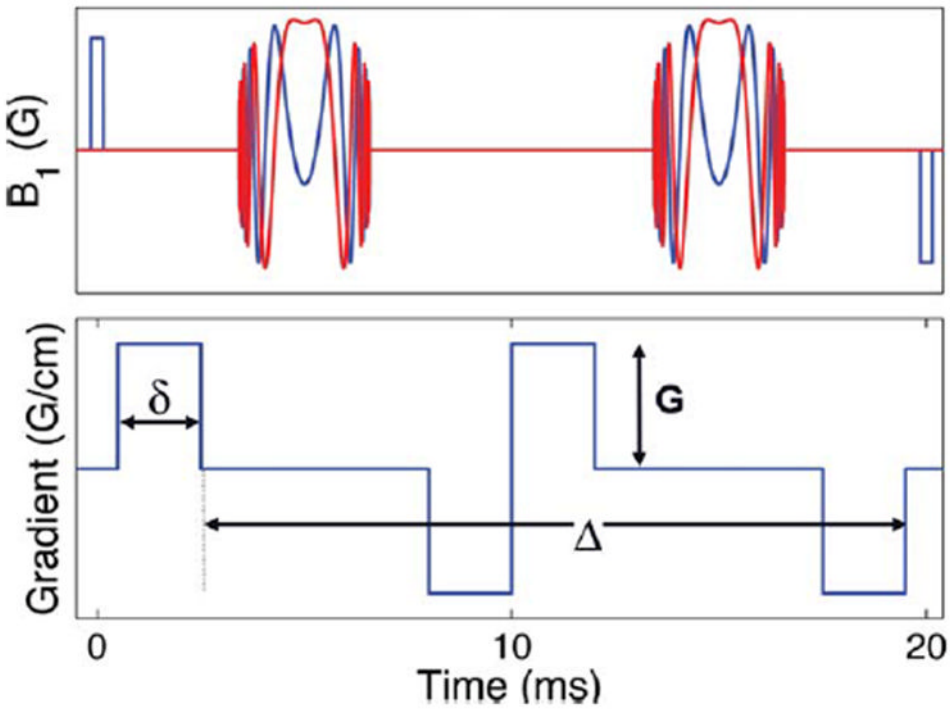

FIG. 3.

Velocity selective module: real (blue) and imaginary (red) RF waveforms (top) and gradient waveform (bottom). Degree of velocity weighting (i.e., the cutoff velocity, V_{CUTOFF}) is defined by the gradient strength (G), gradient duration (δ), and gradient separation (Δ). Disabling velocity selectivity implies $G = 0$. [Color figure can be viewed in the online issue, which is available at wileyonlinelibrary.com.]

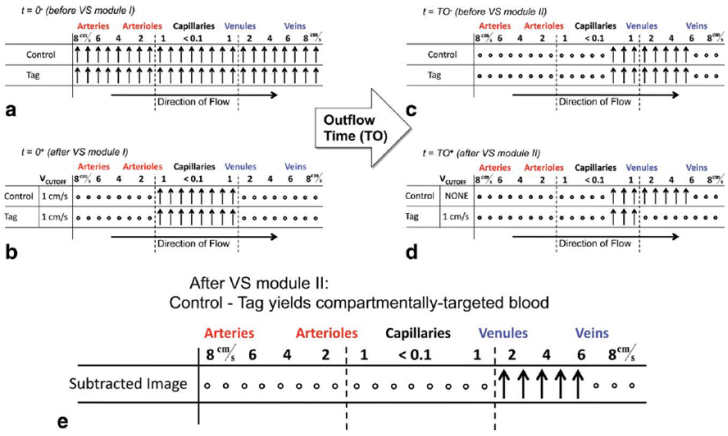

FIG. 4.

Idealized cartoon of venular blood signal targeting in QUIXOTIC approach, as told via spin configuration throughout the experiment. Relaxed spins are denoted by upright arrows; dephased spins by hollow circles. Dotted vertical lines correspond to 1 cm/s blood velocity (i.e., the cutoff velocity in b and d).

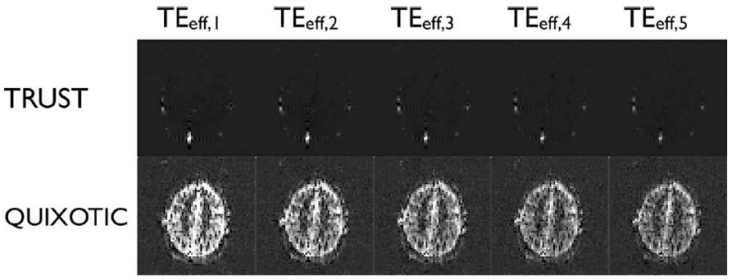

FIG. 5.

TRUST (top) and QUIXOTIC (bottom) mean difference images from representative subject. Mean difference images are an average of many control–tag subtractions and reflect sagittal-sinus blood weighting in TRUST and venular blood weighting in QUIXOTIC.

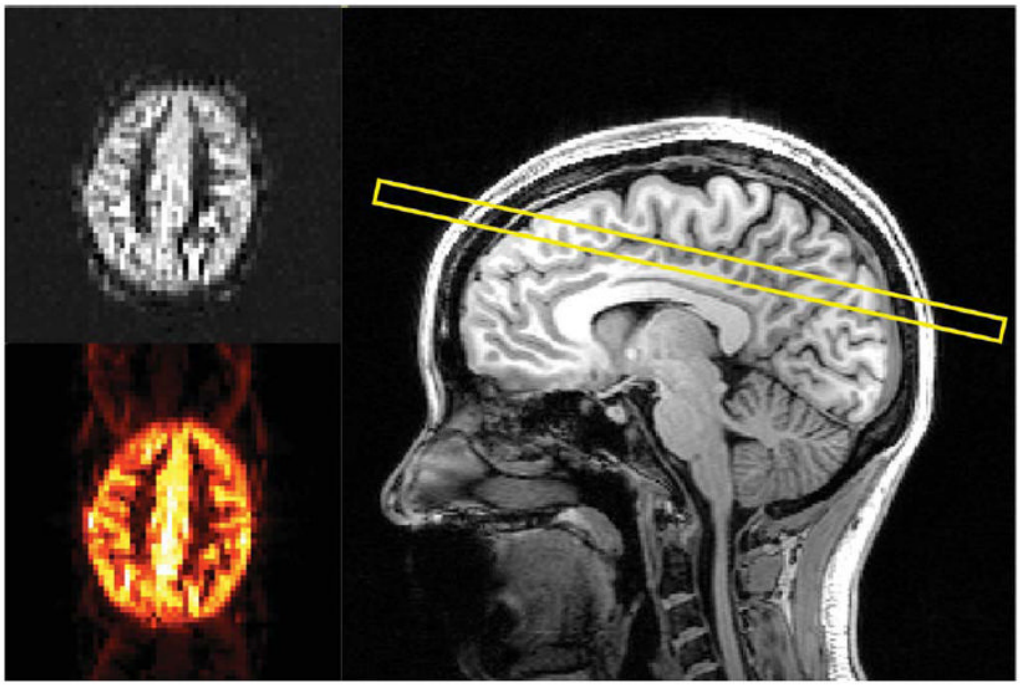

FIG. 6.
Representative CBF image (top-left), DIR image (bottom-left), and anatomical MP-RAGE with prescribed slice overlay (right). QUIXOTIC, ASL, and DIR sequences acquired data in this slice orientation.

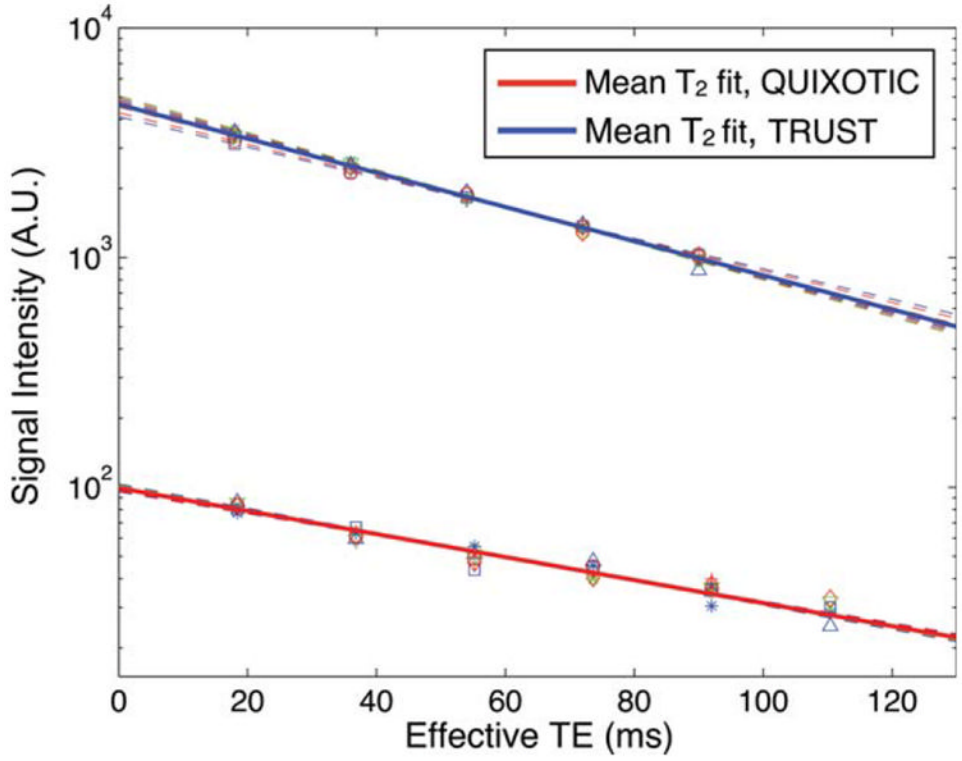

FIG. 7.

TRUST and QUIXOTIC log(SI) versus effective echo time curves and corresponding T_2 fits for all 10 subjects. Vertical offset of the fit lines have been normalized for minimum variance within TRUST and QUIXOTIC datasets. Solid blue and red lines represent mean T_2 fit curves for all 10 subjects, for TRUST and QUIXOTIC, respectively. The vertical intercept estimates the imaging blood volume within sagittal sinus and GM voxels for TRUST and QUIXOTIC, respectively. [Color figure can be viewed in the online issue, which is available at wileyonlinelibrary.com.]

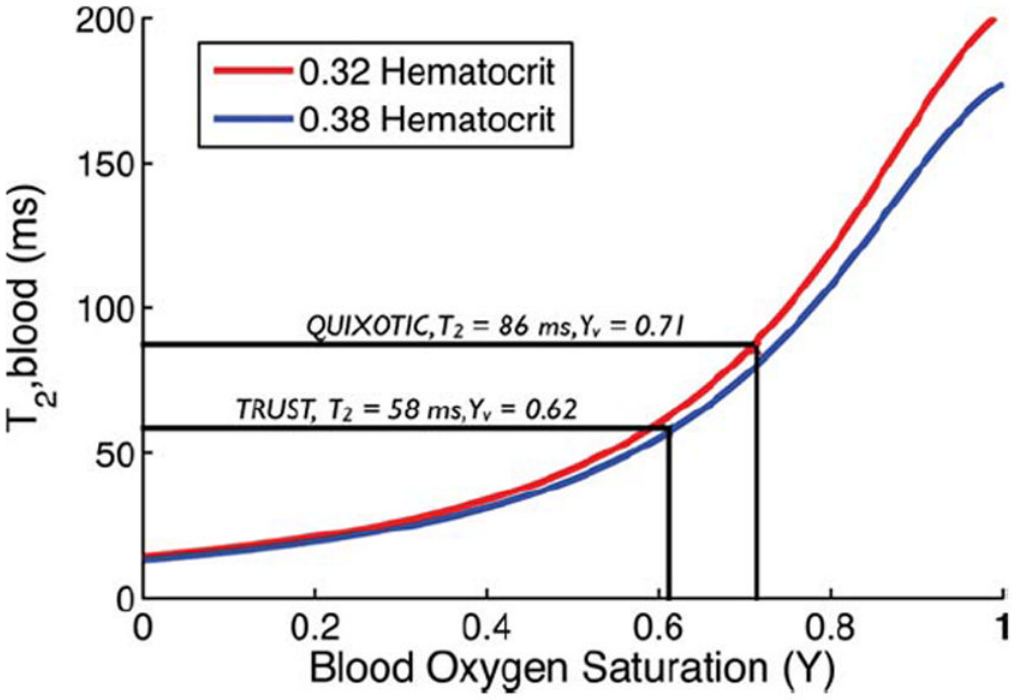

FIG. 8.

Representative T_2 versus Y calibration curves for the representative subject, generated with microvascular (red) and macrovascular (blue) hematocrit, using Eq. 7. These curves are used to calibrate T_2 to blood oxygen saturation for the QUIXOTIC and TRUST experiments. [Color figure can be viewed in the online issue, which is available at wileyonlinelibrary.com.]

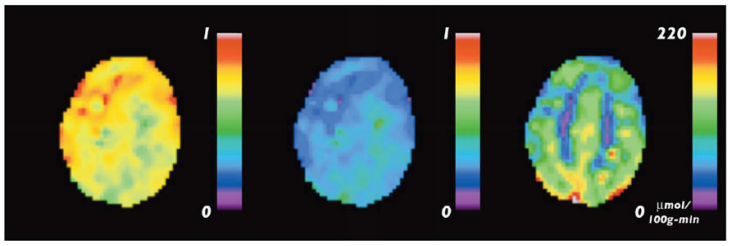

FIG. 9.
Quantitative Y_v (left), OEF (middle), and $CMRO_2$ (right) maps for representative subject, created by applying QUIXOTIC theory on a voxel-by-voxel basis.

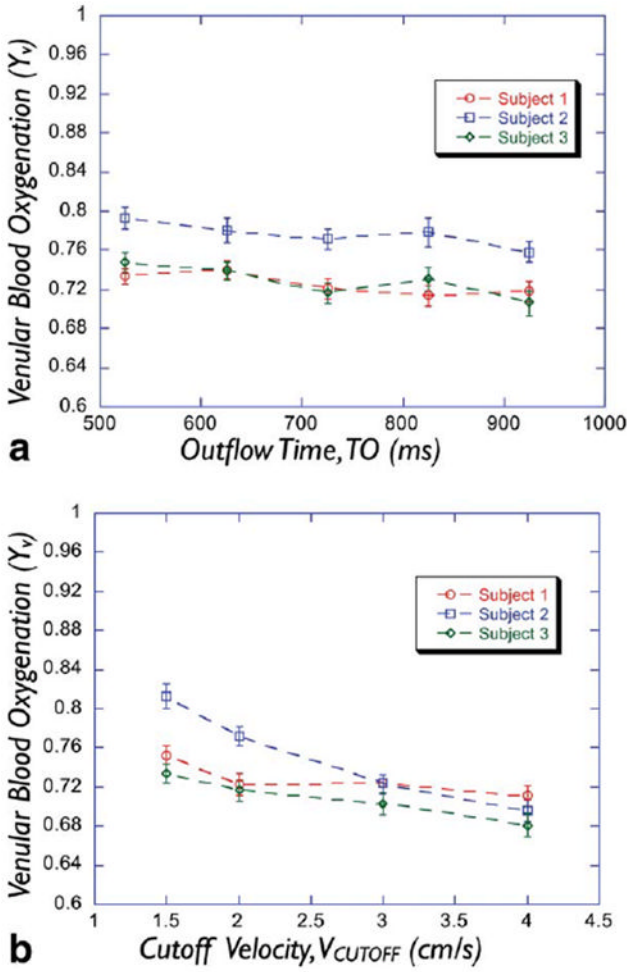

FIG. 10.

Y_v versus TO (**a**) and Y_v versus V_{CUTOFF} (**b**) for the parameter exploration data acquired with turbo QUIXOTIC in three reimaged subjects. Error bars represent the SEE.

Table 1

Summary of QUIXOTIC and TRUST Data for all 10 Volunteers

	QUIXOTIC cortical GM parameters					TRUST whole brain parameters[1]				
Subject	**T_2 (ms) ± SEE**	**GM CBF (mL/100 g min)**	**Y_v**	**OEF**	**GM $CMRO_2$ (μL/100 g min)**	**T_2 (ms) ± SEE**	**WB CBF (mL /100 g min)**	**Y_v**	**OEF**	**WB $CMRO_2$ (μL /100 g min)**
1	91 ± 10	67	0.73	0.25	135	60 ± 1	50	0.63	0.36	144
2	84 ± 5	55	0.70	0.29	124	59 ± 1 5	40	0.62	0.37	116
3	91 ± 6	64	0.75	0.25	140	56 ± 1	48	0.62	0.37	156
4	83 ± 4	52	0.72	0.25	113	55 ± 1	37	0.62	0.35	117
5	83 ± 4	51	0.75	0.24	128	54 ± 1	37	0.63	0.36	138
6	90 ± 9	65	0.73	0.26	141	66 ± 1	48	0.66	0.33	131
7	90 ± 9	42	0.73	0.26	90	57 ± 2	30	0.62	0.37	93
8	86 ± 8	57	0.71	0.29	125	58 ± 1	40	0.62	0.38	118
9	82 ± 8	49	0.72	0.26	116	56 ± 2	35	0.63	0.36	114
10	86 ± 7	55	0.76	0.23	135	63 ± 2	37	0.68	0.32	124
Mean	87	56	0.73	0.26	125	58	40	0.63	0.36	125
Standard deviation	4	8	0.02	0.02	15	4	7	0.02	0.02	18
CV	0.05	0.14	0.03	0.08	0.12	0.07	0.18	0.03	0.06	0.14

Table 2

Test–Retest Data for Subjects 1 and 2

	Subject 1			Subject 2		
	Test	**Retest**	**% Diff**	**Test**	**Retest**	**% Diff**
T_2 (ms)	91	91	0	84	80	5
Y_v	0.73	0.73	0	0.70	0.69	1
OEF	0.25	0.25	0	0.29	0.30	3
$CMRO_2$ (μmol/100 g min)	135	135	0	124	130	5